iScience

CellPress
OPEN ACCESS

Article

A Dendrite-Resistant Zinc-Air Battery

Shangwei Huang, Hui Li, Pucheng Pei, Keliang Wang, Yu Xiao, Chao Zhang, Chen Chen

cchen@tsinghua.edu.cn

HIGHLIGHTS

The ZAB displays an ultralong cycle life (10,000 cycles) at high current density

The ZAB shows high energy densities and an average Coulombic efficiency of ~97.4%

Our ZABs compose energy storage module showing the peak power density of 280.8 mW cm^{-2}

The ZAB has excellent cycle performance, and it can be recovered in time of short circuit

Huang et al., iScience *23*, 101169
June 26, 2020 © 2020
https://doi.org/10.1016/j.isci.2020.101169

iScience

CellPress
OPEN ACCESS

Article

A Dendrite-Resistant Zinc-Air Battery

Shangwei Huang,[1] Hui Li,[2] Pucheng Pei,[1] Keliang Wang,[3] Yu Xiao,[3] Chao Zhang,[2] and Chen Chen[2,4,*]

SUMMARY

Zinc-air batteries (ZABs) have drawn widespread attention for their high energy densities, abundant raw materials, and low cost. However, the issues of metal dendrite formation and air electrode failure have been impeding the development and application of ZABs. Herein, we designed a novel dendrite-resistant ZAB system by adopting multiphase electrolytes to conduct the zinc deposition and the oxygen evolution reaction. The oxygen reduction reaction electrode is kept out of the zinc deposition region to extend the lifespan. The ZABs show an energy density of 1,050.9 Wh kg^{-1} based on the mass of zinc consumption, with an average Coulombic efficiency of ~97.4% in 2,000 h discharge and charge cycling. More impressively, even if a short circuit occurs while charging, the battery can maintain the cycle performance without irreversible failure, which is conducive to the reliability of battery modules and its application in other energy storage/conversion devices.

INTRODUCTION

The intermittent sustainable energy resources such as wind, tidal, and solar energies are crucial for alleviating the potential global energy crisis, and yet are in need of reliable, low-cost, and long-lifespan electrochemical energy storage technologies (Banos et al., 2011; Chu and Majumdar, 2012; Carbajales-Dale et al., 2014; Chu et al., 2017). Zinc-air batteries (ZABs), compared with other options, are promising alternatives for utilizing low-cost, easy-maintenance, and safe water-based electrolytes (Carbajales-Dale et al., 2014; Li and Dai, 2014; Hernandez et al., 2015; Kundu et al., 2016). ZAB systems have a few particular advantages, including high natural abundance of zinc, easy mining, non-toxicity, and the sufficient stability of metallic zinc in water under low redox potentials (Wang et al., 2018a; Schmidt et al., 2019; Zheng et al., 2019). The aqueous electrolytes with high ionic conductivities are conducive to high rate capabilities and durability, suitable for stationary grid storage (Pei et al., 2014; Wang et al., 2018a). However, the prevalent issue of dendrite formation during zinc electrodeposition causes the notorious memory effect and internal short circuit failures (Fu et al., 2017), leading to decline of lifespan (Pei et al., 2014; Kundu et al., 2016; Wang et al., 2018a; Zheng et al., 2019).

To extend the cycling lifespan of ZABs, various strategies have been proposed for the issues of air electrode (Wang et al., 2018b; Najam et al., 2019; Chen et al., 2020) and zinc dendrite (Wang et al., 2018a, 2019a). The methods to optimize cycle performance include substrate epitaxial deposition in a neutral electrolyte (Kundu et al., 2016; Zheng et al., 2019), use of zinc salt with non-aqueous solvents (Pan et al., 2019; Zheng et al., 2019), and development of stable electrocatalysts (You and Hu, 2018; Liu et al., 2019; Wang et al., 2019c; Xu et al., 2019). However, because the electrolyte lacks spatial constraints for zinc deposition, the as-formed zinc tends to grow into stable dendrites under high current density (Li and Dai, 2014; Wang et al., 2019a; Zheng et al., 2019). Thus, it is of great importance for high-rate ZABs to improve the resistance to dendrite formation.

Here we adopt the aqueous multiphase alkaline electrolytes, which are suitable for dendrite control at high current density. As illustrated in Figure 1, the electrolytes are divided into homogeneous and heterogeneous phases by a hydrophilic polytetrafluoroethylene (PTFE) membrane. It is verified by the experiment that zinc deposition is preferential in the heterogeneous phase, and the depositing-stripping region can be restricted in the region. The zinc electrode, as well as an electrode with oxygen evolution reaction (OER) activity, is placed in the heterogeneous phase solution for the charge process. The metal zinc would deposit in the spatially confined heterogeneous phase without entering the homogeneous solution. The air electrode with oxygen reduction reaction (ORR) activity is assembled in the homogeneous phase, and contacts with air for the discharge process. This dendrite-resistant battery delivers energy densities of 196.2

[1]State Key Lab. of Automotive Safety and Energy, Tsinghua University, Beijing 100084, China

[2]Department of Chemistry, Tsinghua University, Beijing 100084, China

[3]School of Mechanical Engineering, Beijing Institute of Technology, Beijing 100081, China

[4]Lead Contact

*Correspondence: cchen@tsinghua.edu.cn

https://doi.org/10.1016/j.isci.2020.101169

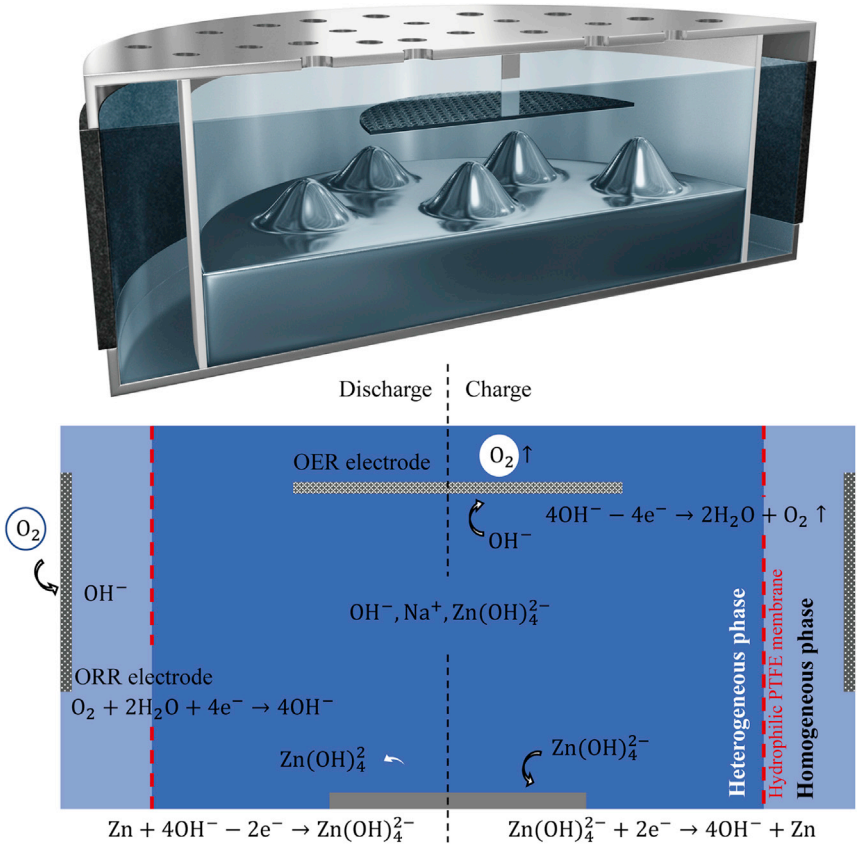

Figure 1. Structure and Design of the ZAB

Schematic illustration and operation principle of the ZAB with multiphase electrolytes: a hydrophilic PTFE membrane divides the solution into homogeneous and heterogeneous phases, and the redox of zinc is carried out in the heterogeneous phase; the OER electrode releases oxygen in heterogeneous phase during charge process, and the ORR electrode consumes oxygen in homogeneous phase during discharge process.

Wh kg^{-1} and 309.1 Wh L^{-1}, calculated according to the mass and volume of battery. The accelerated aging test shows excellent capacity retention as high as 100% after 10,000 rapid cycles at a current density of 50 mA cm^{-2}. In the simulated conditions for utilization of intermittent energy resources, the ZABs maintain a remarkable reliability and responsiveness over the 2,000-h test of discharge and charge cycling, exhibiting great potentials for large-scale energy storage.

Electrochemical Performance of Multiphase Electrolytes

With these configurations of electrolytes, we confirmed that the supersaturated solution (excess ZnO in KOH solution) can be kept apart from a homogeneous solution by a hydrophilic PTFE membrane. As for the durability of the hybrid electrolyte system, the stability of the membrane with two phases was measured in 200-h placement tests. The homogeneous phase exhibits a transparent state, whereas the heterogeneous phase would precipitate and separate. As shown in Figure S1, the hybrid electrolytes were local stable, and the optical images show the high stability of the membrane for electrolyte separation without the exchange of solid substances during the placement test. In Figures 2A and 2B, the PTFE membrane shows a good wettability to water, with the contact angle of 49.9° (initial) and 53.9° (after 200 h), guaranteeing an excellent interface between two phases. The increase in total electrolyte resistance caused by membrane was measured in an h-type electrolytic cell with two platinum electrodes (illustrated in Figure S2). It should be noted that the heterogeneous and homogeneous phases were physically separated; thus the high-frequency impedance indicated the interfacial resistance (Pan et al., 2019; Pei et al., 2014). In Figure S3, the electrochemical impedance spectroscopy result shows the interfacial resistance of 350 mΩ (initial) and ~400 mΩ (after 200 hr). The low interfacial resistance was favorable for fast ion exchange. The compatible interface of different phases provided a stable and long-lifespan hybrid electrolyte system.

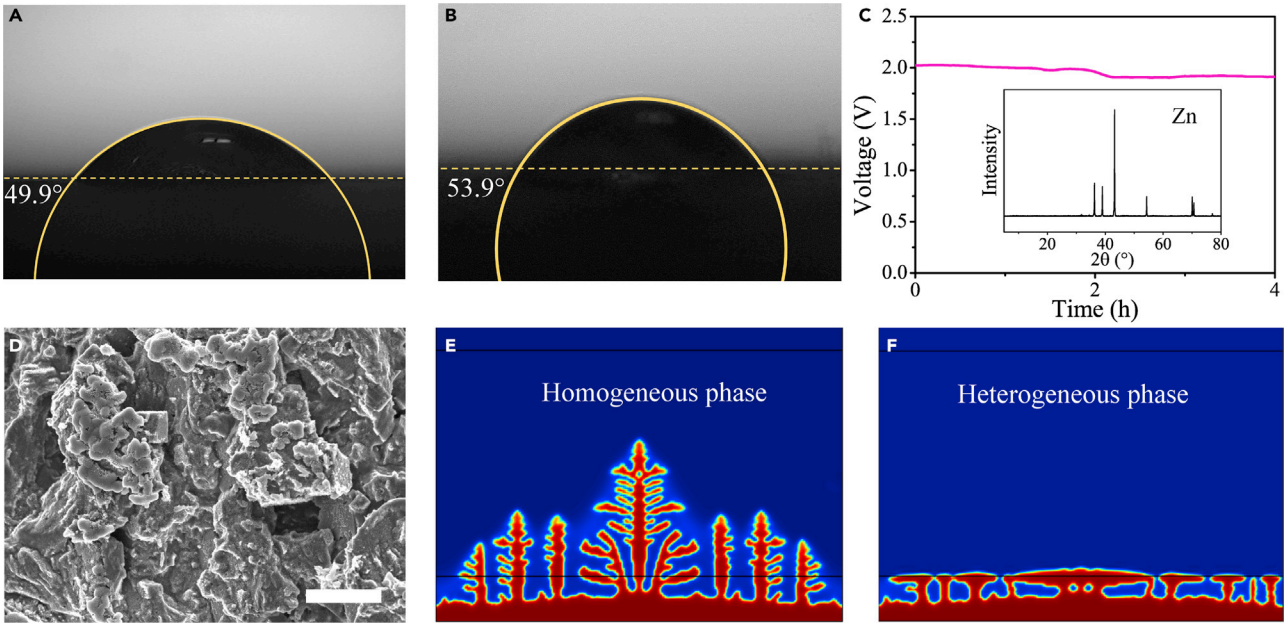

Figure 2. Characteristics of the Zinc Electrodeposited

(A and B) The contact angle image before test (A) and after 200 hours test (B).

(C) The *V-t* curve of zinc electrodeposition at 30 mA cm^{-2}, and the X-ray diffraction pattern of electrodeposition products.

(D) The micromorphology of zinc electrode (scale bar, 2 μm).

(E and F) Simulation results of zinc electrodeposition in (E) homogeneous and (F) heterogeneous phase: the red and blue regions represent the metallic zinc and the electrolyte solution, respectively.

The PTFE membranes were assembled in various simple geometric shapes to conduct the zinc deposition in a heterogeneous phase (see the diagrammatic sketch in Figure S4). The surface for initial zinc deposition was a small disc at the bottom. The homogeneous phase was outside the membranes. The growth direction of zinc was along the membrane. As shown in Figure S5, on the macroscopic view, the electrodeposited zinc tends to fill up the heterogeneous phase region. At the beginning, the metal zinc spread over the disc; then the zinc coating gradually covered the bottom of the heterogeneous phase. The total area of zinc layer was actually increased, contributing to the mitigation of dendrite formation. It was clear that the overpotential was reduced during this process owing to the increase of zinc surface, as shown in Figure 2C. The metal zinc grew along the shape of membrane with a relatively flat upper surface, and grew within the heterogeneous phase without entering the homogeneous phase. Although the electrodeposit was flat, the morphology was porous on microcosmic scale (Figure 2D). The metal zinc was loose and soft, with an average mass density of 0.61 g cm^{-3}, far below the original density of 7.1 g cm^{-3}.

In addition, the PTFE membrane was placed perpendicular to the direction of electrodeposition (sketched in Figure S6). The metal zinc grew through the membrane at 30 mA cm^{-2} and occupied the full space under the membrane (Figure S7). It was clear that the membrane had no hindrance for dendritic growth. The zinc deposition was mainly affected by the growth direction and the phase with high concentration of zinc compounds. The results indicated that the zinc dendrite could be controlled with the multiphase electrolytes by rational guidance for electrodeposition.

In the heterogeneous phase, the insoluble solid particles gradually accumulated on the bottom, forming a porous and loose barrier for zinc electrodeposition. The solid particles brought about the resistance for ionic migration. The ionic conductivity of the heterogeneous phase solution decreased as the concentration of ZnO increased, as shown in Table S1. Finally, there was a stable precipitation layer with poor ionic conductivity on the electrode surface. Because of the loose structure of precipitation, a thin solution film was kept between the electrode and the precipitation layer. That would form a physically isolated environment for dendrite growth. In the thin solution film, the electrodeposition would still tend to form dendrites at high current density. Then the dendrite reached the precipitation layer soon, and the electrodeposition rate was slowed down at the top of the dendrite. The especially prominent dendrite was inhibited, forming a relatively flat surface.

To gain in-depth insights on the dendritic growth of electrodeposited zinc in a heterogeneous phase, the phase-field method was utilized to investigate the electrodeposition process (Wang et al., 2019a). As illustrated in Figure S8, the zinc was generated at the bottom edge. In addition, a ZnO layer with low ionic conductivity was located above the bottom edge. A reaction area without the ZnO layer (homogeneous phase) was used for comparison. The electrodeposition current density was set as 30 mA cm^{-2}. The ZnO is soluble in the alkaline electrolyte such as sodium hydroxide solution with a low solubility (Dirkse et al., 1954):

$$ZnO + H_2O + 2OH^- \rightleftharpoons Zn(OH)_4^{2-}$$

In the homogeneous system, all the ZnO dissolved in the electrolyte, converting to zincate ions. The growth of zinc dendrite was almost uncontrollable. In the heterogeneous phase electrolyte, the majority of ZnO precipitated in the insoluble solid state (Dirkse et al., 1954). In the process of zinc deposition, the zincate ions were consumed at the zinc electrode, whereas the porous precipitation layer provided zincate ions by dissolution. This structure maintained a high concentration of zincate ions and high mass transfer resistance at the zinc electrode. The growth of zinc dendrites toward the precipitated layer was inhibited.

The simulation results were shown in Figures 2E and 2F. In the space between ZnO layer and bottom edge, zincate ions would be reduced and deposited on the electrode surface. At the high current density, electrochemical reaction kinetics, atomic bond, ion diffusion, crystal nucleation, and growth all have a critical impact on the morphology of electrodeposited zinc. It was expected that the classical dendrite was unrestricted and got expanded in the thin solution film (Figure S8). The tip of dendrite slowed the growth when it reached the ZnO layer, resulting in promoted crossing growth. As the result of the strengthening crossing growth, the space under ZnO layer was gradually filled with the dendritic metal zinc. The microscopic morphology was dendrite, whereas the macroscopical structure had a flat surface. The ZnO reduced the ionic conductivity in the heterogeneous phase, but improved the space utilization of zinc deposition. The deposited microstructure was still dendritic, similar to that deposited in homogeneous phase, leading to the low mass density. Fortunately, the macroscopic shape tended to be well ordered. Compared with the morphology of random dendrites deposited in homogeneous phase, the macroscopic shape could be predicted because of the flat upper surface, which was deposited in heterogeneous phase. The ordered electrodeposition contributed to preventing the internal short circuiting of ZABs.

Fabrication and Stability of the Air Electrode

The oxygen reduction reaction needs a reaction environment including electron conductor, ionic conductor, and oxygen path. Gaseous oxygen is the product of OERs (Ma and Wang, 2014; Fu et al., 2017; Tang et al., 2017; Wang et al., 2019b; Sun et al., 2020); thus the oxygen path is not necessary for the oxygen evolution process (Sun et al., 2020). Consequently, we could accurately regulate and control the redox of oxygen in ZABs. The classic structure of the air electrode includes electrocatalysis layer, collector layer, and gas diffusion layer (Li and Dai, 2014; Fu et al., 2017; Wang et al., 2018c; Xing et al., 2019). With the alkaline electrolyte of ZABs, we adopted two types of air electrodes to evaluate their durability at high current density: a separated type and an integrated type. To match the multiphase electrolytes, we designed an air electrode only with commercial Pt electrocatalyst for ORR and an extra porous electrode coated with IrO_2 for OER (separated type). The other type of air electrode integrated commercial bifunctional electrocatalysts of Pt/IrO_2 in the electrocatalysis layer (integrated type). Both types of air electrode displayed high reversibility for the redox of oxygen, with charge-discharge voltage polarization of 0.67 V (separated type) and 0.65 V (integrated type) at 20 mA cm^{-2} respectively, as shown in Figure 3C.

The integrated air electrode was assembled in a symmetrical electrolytic cell with 1 M NaOH. The air electrodes were in contact with air and electrolyte, with one as anode and the other as cathode (as illustrated in Figure 3A). The separated air electrodes directly constituted two electrodes of the electrolytic cell because of its asymmetry, and the OER electrode was in the electrolyte solution, serving as the anode (as illustrated in Figure 3B). The durability tests were conducted under constant current (30 mA cm^{-2}) and rectangular wave current conditions. In constant current tests, the separated air electrode was more stable than the integrated type. As shown in Figure 3D, the voltages of both types of air electrodes increased after 200 h, with an increment of 60 mV for the integrated type and 170 mV for the separated type. Although the overpotential of both types of air electrode increased, the separated air electrode was more stable. In the rectangular wave current tests, the integrated air electrode suffered from a more significant voltage rise, whereas the separated counterpart could maintain stable voltage characteristics. The results showed that the integrated air electrode had a lower stability owing to some irreversible failure in the redox of oxygen (Figure 3E). When the air electrodes acted as the cathode, the surfaces of the

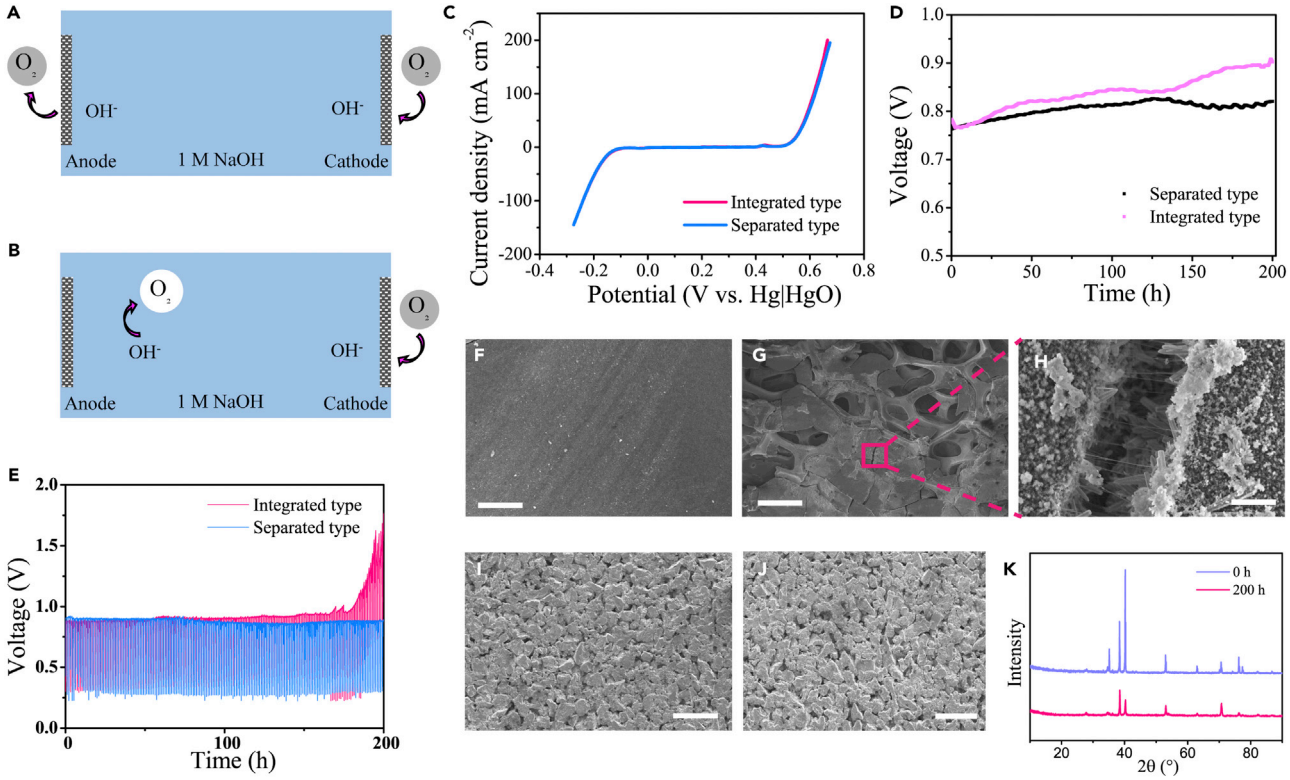

Figure 3. Stability Tests of Air Electrodes

(A and B) The diagrammatic sketch of the integrated (A) and separated (B) air electrode in an electrolytic cell.

(C) The polarization characteristics of integrated and separated air electrode.

(D and E) The *u-t* curve of both air electrodes at 30 mA cm^{-2}. (E). The *u-t* curves of both air electrodes at rectangular wave current: 50 mA cm^{-2} for 50 min, 0 mA cm^{-2} for 10 min.

(F–H) Scanning electron microscopic (SEM) images of the integrated air electrode working as anode in a symmetrical electrolytic cell before (F) and after (G and H) the rectangular wave current test. Scale bars: 50 μm in (F), 200 μm in (G), and 2 μm in (H).

(I and J) SEM images of the separated air electrode working as anode in a symmetrical electrolytic cell before (I) and after (J) the rectangular wave current test. Scale bars, 1 mm

(K) X-ray diffraction patterns of the separated air electrode working as anode before and after the rectangular wave current test.

electrocatalysis layer were nearly unchanged in both types of air electrodes (Figure S9). Some small cracks could have formed during the installation or sample preparation. When the air electrodes served as the anode, the separated air electrode still stayed relatively unchanged (Figures 3I and 3J), and the X-ray diffraction patterns verified the high stability of the components (Figure 3K). There was significant structural damage in the electrocatalysis layer of the integrated air electrode. As shown in Figures 3F–3H, it was clear that there was massive material loss on the surface, and even partial exposure of the collector layer. The activity of the electrocatalysis layer declined as the electrocatalysts separated from the electrode, resulting in an increased overpotential.

The mechanical failure would further lead to the performance degradation of the integrated air electrode. The material loss changed the electrode structure and components, thus increasing the risk of battery failure such as electrolyte leakage (Li and Dai, 2014). The results showed the separated air electrode would be better suited for the multiphase electrolytes.

Cyclability Performance of the ZAB

Figure 1 illustrates the structure and the operating principle of the ZABs, and Figure S11 illustrates the electrical connection of the separated ORR/OER electrodes to the external load. The batteries were improved on the basis of the button cell, as shown in Figure S10. A hydrophilic PTFE membrane divided the electrolyte solution into homogeneous and heterogeneous phases. Both zinc deposition and stripping occurred in the heterogeneous phases. The separated air electrode was used for ORR in homogeneous phase and for OER in heterogeneous

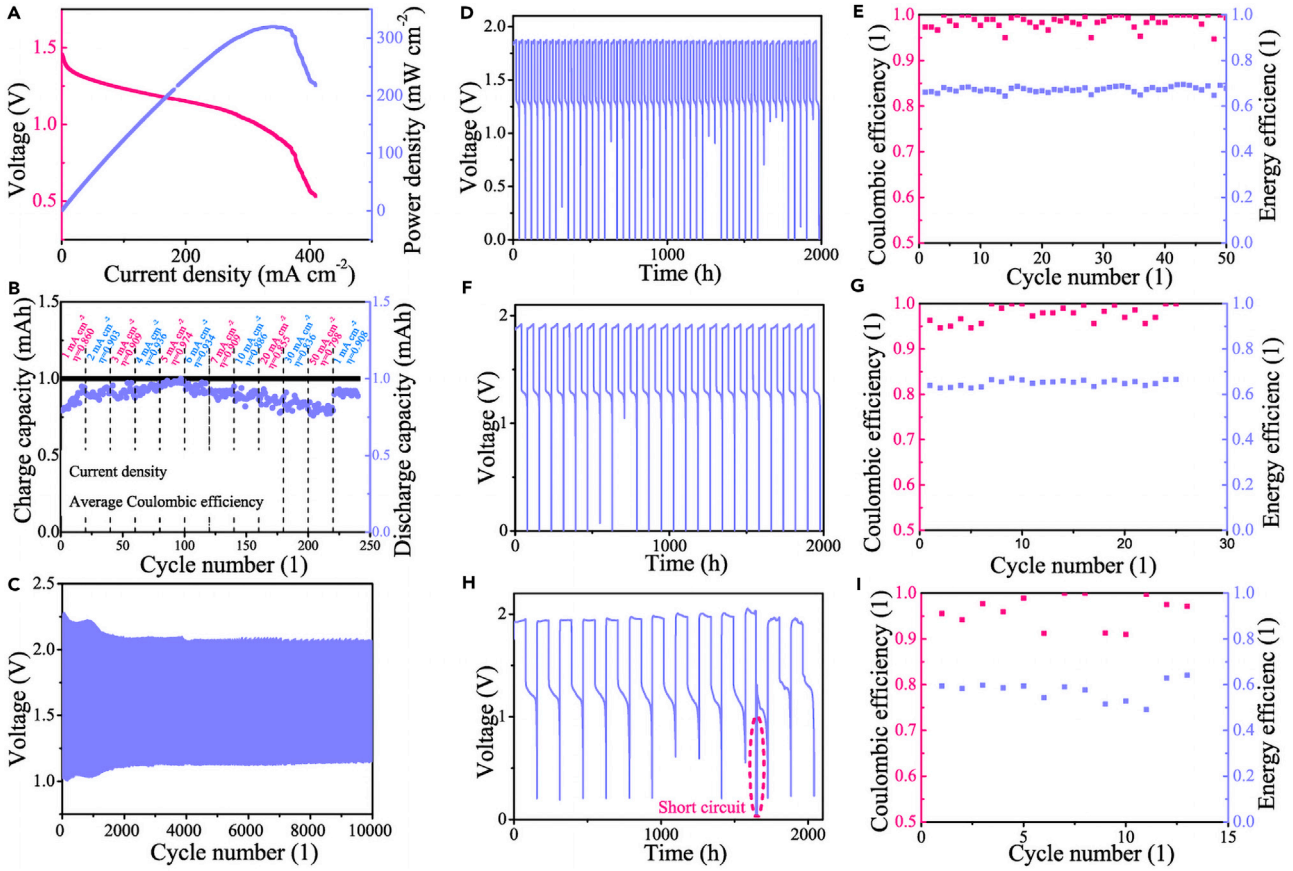

Figure 4. Performance Tests of the ZAB

(A) Discharge characteristics of ZAB.

(B) The Coulombic efficiencies of the ZAB under different current densities: 1, 2, 3, 4, 5, 6, 7, 10, 20, 30, and 50 mA cm^{-2}.

(C) The cyclability performance of the ZAB (charge 1 min and discharge 1 min at 50 mA cm^{-2}).

(D and E) The voltage characteristics (D) and Coulombic and energy efficiencies (E) of the ZAB at 5 mA cm^{-2} with capacity density of 100 mAh cm^{-2}.

(F and G) The voltage characteristics (F) and Coulombic and energy efficiencies (G) of the ZAB at 5 mA cm^{-2} with capacity density of 200 mAh cm^{-2}.

(H and I) The voltage characteristics (H) and Coulombic and energy efficiencies (I) of the ZAB at 5 mA cm^{-2} with capacity density of 400 mAh cm^{-2}.

phase. The hydrogen evolution was a competitive side reaction in the zinc deposition process, which would reduce the charge-discharge efficiency. Considering the narrow electrochemical window of aqueous electrolyte, sodium stannate was used as electrolyte additive to inhibit hydrogen evolution (Kundu et al., 2016).

In a fully charged state, the discharge current-voltage curve of ZABs was shown in Figure 4A. The ZAB had a stable open-circuit voltage of 1.46 V and a peak power density up to 320.2 mW cm^{-2} (at the current density of 339.8 mA cm^{-2}). In the actual state, the oxygen concentration was lower than that of pure oxygen, and the electrocatalysts were insufficient to maintain the ORR/OER perfectly reversible. The hydrogen evolution reaction would raise the potential of the zinc electrode. These factors lead to the open-circuit voltage being lower than the theoretical value.

Because of the hydrogen evolution reaction, charging at high current density as well as discharging at low current density could be beyond the electrochemical window and increase the possibility of side reaction. There should exist an optimum charge-discharge current density to attain the highest Coulombic efficiency (Zheng et al., 2019). The charge capacity was set as 1 mAh, and Figure 4B showed the discharge capacities at different current densities (1–7, 10, 20, 30, 50 mA cm^{-2}). The results indicated the highest average Coulombic efficiency of 97.4% at 5 mA cm^{-2}. In the accelerated tests of durability for ZAB, the fully charged battery was operated at the current density of 50 mA cm^{-2} for 10,000 cycles. Under such high rate conditions, Figure 4C showed that the ZAB had a stable charge-discharge voltage polarization about 1 V, without any significant increase.

The cyclability performance of the ZAB was conducted at the current density of 5 mA cm^{-2} with different capacity densities (100, 200, 400 mAh cm^{-2}). The ZAB exhibited excellent reversibility and stability with these capacity densities in the 2,000-h discharge and charge cycling, as shown in Figures 4D–4I. The voltage curves indicated that the ZAB maintained the average Coulombic efficiencies above 90% without an internal short circuit caused by dendrite except at 400 mAh cm^{-2}, and exhibited the minimum charge-discharge voltage polarization of 0.6 V. During the test, the highest energy efficiency was 69.6%. The battery realized the high energy density of 1,050.9 Wh kg^{-1} based on the mass of zinc consumption. With the total mass of ZAB included (Table S2), the battery showed a discharge energy density of 309.1 Wh L^{-1} and 196.2 Wh kg^{-1}.

In Figures 4D, 4F, and 4H, the point from discharge to charge process showed drop-points close to zero. During the discharge process, the metal zinc was oxidized and the amount of metal zinc kept decreasing. At the end of the discharge process, there was hardly any metal zinc in the zinc electrode. Owing to the state change of the zinc electrode, the dynamic equilibrium of the electrochemical reaction was broken, and the voltage of the battery would drop to the voltage limit.

In the deep charging and discharging active status (400 mAh cm^{-2}), the voltage curve dropped to near zero during charge process in the 11th cycle (Figure 4H). Apparently, there was an internal short circuit caused by the dendrite. The supersaturated solution turned homogeneous because the ZnO precipitate was dissolved and the dendrite formation became uncontrollable. Nevertheless, the cyclability performance of the ZAB seemed uncompromised. The discharge process following the internal short circuit was highly effective, and the following cycles were stable and reversible. The ZAB was resistant to dendrite and supported fault recovery without manual intervention, benefiting from the multiphase electrolytes and separated air electrode. As demonstrated by the experimental and theoretical methods, the zinc deposition was spatially limited, and the dendrite growth was inhibited in the heterogeneous phase. The ORR electrode got rid of the short circuit, even though the dendrite contacted with OER electrode, thus guaranteeing the high reliability for cycle operation.

Applications of the ZABs in Intermittent Energy Storage

In large-scale energy storage with high capacity requirements, the batteries are composed of modules in series and parallel forms. We used two ZABs in series connection for intermittent energy storage with a simulated condition: 12 h charge and 12 h discharge at 30 mA cm^{-2}. The capacity density was 360 mAh cm^{-2}, avoiding the heterogeneous phase to turn homogeneous at deep charging and discharging active status.

The ZAB module was stable with an open-circuit voltage of 2.89 V (Figure 5A). The total discharge polarization curve showed the peak power density of 280.8 mW cm^{-2} (at the current density of 383.6 mA cm^{-2}). The discharge performance characteristics could be approximately regarded as the linear superposition of independent ZABs, and the connected components mainly caused the performance penalty. The module exhibited the highest energy efficiency of 62.0% (Figure 5B). This ZAB module operated continuously for 60 days without any halt, as shown in Figure 5C. Because of the dendrite-resistant ZABs, the module exhibited the ideal energy storage characteristics of steady operation, anti-overloading, and free maintenance (compared with other zinc-air counterparts in Table S3).

Conclusions

In summary, we demonstrated experimentally and computationally the ZAB with high energy density, high reliability, and dendrite resistance. Benefiting from the form of separated air electrode, each electrode had a very small potential change in operation, improving the stability. The zinc deposition could be conducted in the heterogeneous phase separated with ORR electrode. Although the loose and dendritic microstructure seemed inevitable at high current density (30 mA cm^{-2}), the growth of metal zinc exhibited a good controllability at the macroscopic level with a relatively flat upper surface. Even when the internal short circuit occurred during charging process, the ZAB would get auto recovery and keep the cyclability performance. This work sheds light on the effective strategy of controlled zinc deposition, widening the way to the applications of the ZABs in large-scale energy storage with high energy density, high safety, anti-overloading, and free maintenance.

Limitations of the Study

Our work has demonstrated how the separated air electrode matched with multiphase electrolytes for ZABs can resist dendrite formation and lead to the ultralong cycle life of the ZAB. However, the battery performance is mainly revealed and characterized by electrochemical analysis, which lacks a deeper understanding of the anti-dendritic mechanism. It requires *in situ* technology and first-principles study for further analysis.

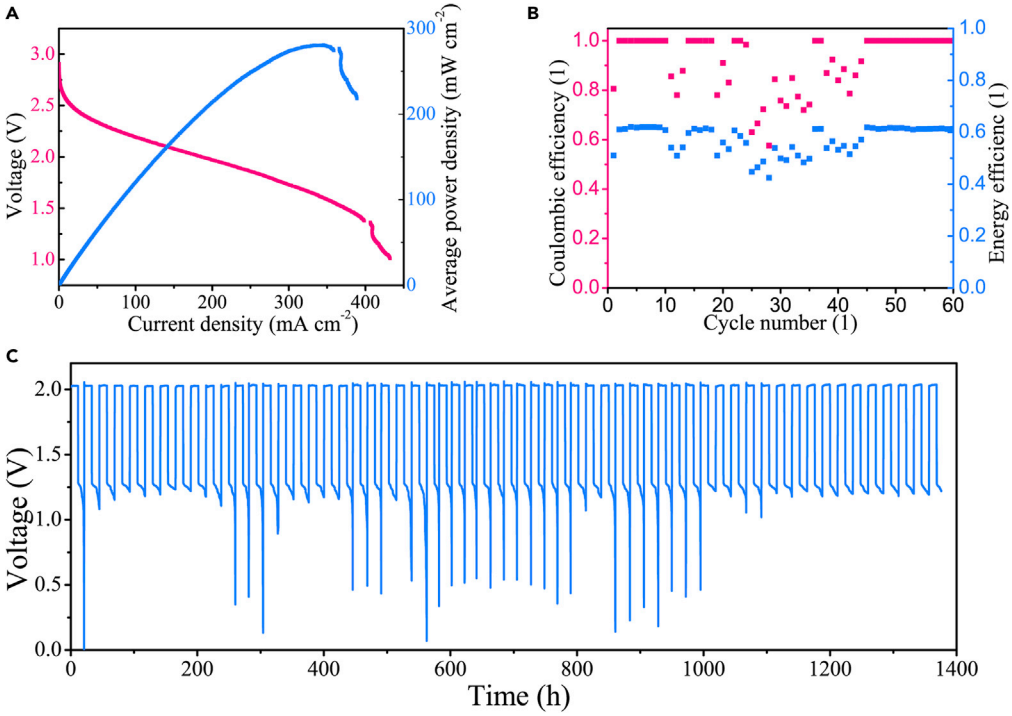

Figure 5. Performance Tests of the ZAB Module

(A) Discharge characteristics of ZAB module.

(B) The Coulombic and energy efficiencies of ZAB module at current density of 30 mA $cm^{-2}$and capacity density of 360 mAh cm^{-2} in 60-day simulated condition.

(C) The *u-t* curve of ZAB module during the 60-day simulated condition.

Resource Availability

Data and Code Availability

The data that support the findings of this study are available from the corresponding authors upon reasonable request.

Lead Contact

Chen Chen cchen@tsinghua.edu.cn.

Materials Availability

The materials that support the findings of this study are available from the corresponding authors upon reasonable request.

METHODS

All methods can be found in the accompanying Transparent Methods supplemental file.

SUPPLEMENTAL INFORMATION

Supplemental Information can be found online at https://doi.org/10.1016/j.isci.2020.101169.

ACKNOWLEDGMENTS

This work was supported by the National Key Research and Development Program of China (Nos. 2017YFB0102705, 2016YFB0101305 and 2016YFB0101208, 2018YFA0702003), National Natural Science Foundation of China (No. 21975143, 21706013, 21676158, 21890383, 21925202), Beijing Natural Science Foundation (JQ18007), and Tsinghua University Initiative Scientific Research Program.

AUTHOR CONTRIBUTIONS

S.H. conceived the idea. S.H. and H.L. carried out the sample preparation, characterization battery assembly, and electrochemical test. S.H. and H.L. obtained the data of contact angle, XRD, and SEM. S.H., C.Z. and H.L. wrote the manuscript. Y.X. and K.W. carried out the simulation of dendrite growth. S.H., H.L., K.W., C.C., and P.P. discussed the electrochemical process and gave useful suggestions. All the authors contributed to overall scientific interpretation and edited the manuscript. S.H. and H.L. contributed equally to this work.

DECLARATION OF INTERESTS

The authors declare no conflicts of interest.

Received: February 12, 2020
Revised: April 7, 2020
Accepted: May 13, 2020
Published: June 26, 2020

REFERENCES

Banos, R., Manzano-Agugliaro, F., Montoya, F., Gil, C., Alcayde, A., and Gómez, J. (2011). Optimization methods applied to renewable and sustainable energy: a review. Renew. Sustain. Energ. Rev. *15*, 1753–1766.

Carbajales-Dale, M., Barnhart, C.J., Brandt, A.R., and Benson, S.M. (2014). A better currency for investing in a sustainable future. Nat. Clim. Change *4*, 524.

Chen, C., Cheng, D., Liu, S., Wang, Z., Hu, M., and Zhou, K. (2020). Engineering the multiscale structure of bifunctional oxygen electrocatalyst for highly efficient and ultrastable zinc-air battery. Energy Storage Mater. *24*, 402–411.

Chu, S., Cui, Y., and Liu, N. (2017). The path towards sustainable energy. Nat. Mater. *16*, 16.

Chu, S., and Majumdar, A. (2012). Opportunities and challenges for a sustainable energy future. Nature *488*, 294.

Dirkse, T.P., Postmus, C., Jr., and Vandenbosch, R. (1954). A study of alkaline solutions of zinc oxide. J. Am. Chem. Soc. *76*, 6022–6024.

Fu, J., Cano, Z.P., Park, M.G., Yu, A., Fowler, M., and Chen, Z. (2017). Electrically rechargeable zinc–air batteries: progress, challenges, and perspectives. Adv. Mater. *29*, 1604685.

Hernandez, R.R., Hoffacker, M.K., and Field, C.B. (2015). Efficient use of land to meet sustainable energy needs. Nat. Clim. Change *5*, 353.

Kundu, D., Adams, B.D., Duffort, V., Vajargah, S.H., and Nazar, L.F. (2016). A high-capacity and long-life aqueous rechargeable zinc battery using a metal oxide intercalation cathode. Nat. Energy *1*, 16119.

Li, Y., and Dai, H. (2014). Recent advances in zinc–air batteries. Chem. Soc. Rev. *43*, 5257–5275.

Liu, C., Dong, F., Wu, M., Wang, Y., Xu, N., Wang, X., Qiao, J., Shi, P., and Huang, H. (2019). Dual-active-sites design of CoS_x anchored on nitrogen-doped carbon with tunable mesopore enables efficient Bi-Functional oxygen catalysis for ultra-stable zinc-air batteries. J. Power Sources *438*, 226953.

Ma, H., and Wang, B. (2014). A bifunctional electrocatalyst α-MnO_2-$LaNiO_3$/carbon nanotube composite for rechargeable zinc–air batteries. RSC Adv. *4*, 46084–46092.

Najam, T., Shah, S.S.A., Ding, W., Deng, J., and Wei, Z. (2019). Enhancing by nano-engineering: hierarchical architectures as oxygen reduction/evolution reactions for zinc-air batteries. J. Power Sources *438*, 226919.

Pan, Z., Yang, J., Zang, W., Kou, Z., Wang, C., Ding, X., Guan, C., Xiong, T., Chen, H., and Zhang, Q. (2019). All-solid-state sponge-like squeezable zinc-air battery. Energy Storage Mater. *23*, 375–382.

Pei, P., Wang, K., and Ma, Z. (2014). Technologies for extending zinc–air battery's cyclelife: a review. Appl. Energy *128*, 315–324.

Schmidt, T.S., Steffen, B., Egli, F., Pahle, M., Tietjen, O., and Edenhofer, O. (2019). Adverse effects of rising interest rates on sustainable energy transitions. Nat. Sustainability *2*, 879–885.

Sun, H., Li, Q., Lian, Y., Zhang, C., Qi, P., Mu, Q., Jin, H., Zhang, B., Chen, M., and Deng, Z. (2020). Highly efficient water splitting driven by zinc-air batteries with a single catalyst incorporating rich active species. Appl. Catal. B: Environ. *263*, 118139.

Tang, Q., Wang, L., Wu, M., Xu, N., Jiang, L., and Qiao, J. (2017). Achieving high-powered Zn/air fuel cell through N and S co-doped hierarchically porous carbons with tunable active-sites as oxygen electrocatalysts. J. Power Sources *365*, 348–353.

Wang, F., Borodin, O., Gao, T., Fan, X., Sun, W., Han, F., Faraone, A., Dura, J.A., Xu, K., and Wang, C. (2018a). Highly reversible zinc metal anode for aqueous batteries. Nat. Mater. *17*, 543.

Wang, H.-F., Tang, C., Wang, B., Li, B.-Q., Cui, X., and Zhang, Q. (2018b). Defect-rich carbon fiber electrocatalysts with porous graphene skin for flexible solid-state zinc–air batteries. Energy Storage Mater. *15*, 124–130.

Wang, K., Pei, P., Wang, Y., Liao, C., Wang, W., and Huang, S. (2018c). Advanced rechargeable zinc-air battery with parameter optimization. Appl. Energ. *225*, 848–856.

Wang, K., Xiao, Y., Pei, P., Liu, X., and Wang, Y. (2019a). A phase-field model of dendrite growth of electrodeposited zinc. J. Electrochem. Soc. *166*, D389–D394.

Wang, P., Wan, L., Lin, Y., and Wang, B. (2019b). Construction of mass-transfer channel in air electrode with bifunctional catalyst for rechargeable zinc-air battery. Electrochimica Acta *320*, 134564.

Wang, T., Wu, J., Liu, Y., Cui, X., Ding, P., Deng, J., Zha, C., Coy, E., and Li, Y. (2019c). Scalable preparation and stabilization of atomic-thick CoNi layered double hydroxide nanosheets for bifunctional oxygen electrocatalysis and rechargeable zinc-air batteries. Energy Storage Mater. *16*, 24–30.

Xing, Z., Deng, Y.-P., Sy, S., Tan, G., Li, A., Li, J., Niu, Y., Li, N., Su, D., and Lu, J. (2019). Carbon-pore-sheathed cobalt nanoseeds: an exceptional and durable bifunctional catalyst for zinc-air batteries. Nano Energy *65*, 104051.

Xu, N., Zhang, Y., Wang, M., Fan, X., Zhang, T., Peng, L., Zhou, X.-D., and Qiao, J. (2019). High-performing rechargeable/flexible zinc-air batteries by coordinated hierarchical Bi-metallic electrocatalyst and heterostructure anion exchange membrane. Nano Energy *65*, 104021.

You, T.-H., and Hu, C.-C. (2018). Designing binary Ru–Sn oxides with optimized performances for the air electrode of rechargeable zinc–air batteries. ACS Appl. Mater. Interfaces *10*, 10064–10075.

Zheng, J., Zhao, Q., Tang, T., Yin, J., Quilty, C.D., Renderos, G.D., Liu, X., Deng, Y., Wang, L., and Bock, D.C. (2019). Reversible epitaxial electrodeposition of metals in battery anodes. Science *366*, 645–648.

iScience, Volume *23*

Supplemental Information

A Dendrite-Resistant Zinc-Air Battery

Shangwei Huang, Hui Li, Pucheng Pei, Keliang Wang, Yu Xiao, Chao Zhang, and Chen Chen

A dendrite-resistant zinc–air battery

Shangwei Huang[1], Hui Li[2], Pucheng Pei [1]*, Keliang Wang[3], Yu Xiao[3], Chao Zhang[2] and Chen Chen[2]*

[1] State Key Lab. of Automotive Safety and Energy, Tsinghua University, Beijing 100084, China.

[2] Department of Chemistry, Tsinghua University, Beijing 100084, China.

[3] School of Mechanical Engineering, Beijing Institute of Technology, Beijing 100081, China.

Transparent Methods

Preparation of air electrode

The integrated air electrodes were prepared by the typical hot-presses process(Fu et al., 2017, Li et al., 2017). The electrocatalysts (Pt and IrO_2) were purchased from Shanghai Hesen Electric Co., Ltd. The platinum content was 1 mg cm^{-2}; the iridium dioxide content was 1 mg cm^{-2}.

The ORR electrodes of separated air electrodes were prepared as the integrated air electrodes, Pt as an electrocatalyst. The OER electrodes were porous titanium coated with IrO_2 (1 mg/cm^2, Shanghai Hesen Electric Co., Ltd).

Assembly of battery

The hydrophilic PTFE membranes were purchased from Membrane Solution Technology Co., Ltd. A circular nick foil served as the zinc electrode collector, coated by PTFE insulating film with a reaction area of 1 cm^2. The ORR electrode surrounded the zinc electrode, and separated with the hydrophilic PTFE membrane. The OER electrode (1 cm^2) was fixed in a commercial button battery case with 17 holes. The compositions of electrolytes blend were H_2O (33 wt%), NaOH (40 wt%), ZnO (26 wt%), and Na_2SnO_3 (1 wt%). Then the electrolytes were injected. It should be noted that the battery was assembled in the charge state of 0 %.

Characterization methods

Scanning electron microscopy (SEM) and energy dispersion spectroscopy (EDS) were performed on a field-emission scanning electron microscope (Zeiss Merlin). The samples were directly put on the sample stage with conductive tape. X-ray diffraction (XRD) measurement was carried out on PHI Quantro SXM (ULVAC-PHI) instrument. The contact angle measurement for H_2O on the hydrophilic PTFE membrane was carried out on the video contact angle measuring instrument (Dataphysics OCA25). The charge–discharge tests were conducted with the battery tester (5 V, 50mA, Neware Technology Limited.)

Dendrite growth simulation

The computational simulation was conducted on the Matlab (R2016b). As reported in our previous work(Wang et al., 2019a), a phase-field model of electrodeposited zinc was established to study the mechanism of dendritic growth in multiphase electrolytes. In the heterogeneous phase, the insoluble solid powders of ZnO precipitate form a porous layer, which increases the resistance of

charge transfer and crystal growth. In a two-dimensional square (10 mm X 10 mm), there was a 1 mm thickness solution film between the ZnO layer and the bottom boundary. The zinc grew with the initial nucleation at the midpoint of the bottom boundary. The current density was 30 mA cm^{-2}.

The phase-field model assumes that the electrode–electrolyte interface migration is proportional to interfacial free energy as well as electric energy, which is based on phase transformation theory of Ginzburg–Landau together with the Butler–Volmer equation. The simulation results were obtained by coupling three governing equations of a phase-change equation (1), an ion diffusion equation (2) and charge conservation (3).

$$\frac{\partial \Upsilon}{\partial t} = -L_\sigma \left[\frac{\partial G(\Upsilon)}{\partial \Upsilon} + \nabla\left(\kappa \nabla \Upsilon\right) \right] - L_\sigma H'(\Upsilon) \left[H(\Upsilon) \cdot \exp\left(\frac{\alpha z F \eta}{RT} \right) - \left(1 - H(\Upsilon)\right) \cdot \exp\left(-\frac{(1-\alpha) z F \eta}{RT} \right) \right] \quad (1)$$

where Υ is the order parameter of the liquid–solid interface; L_σ is interface mobility; η is zinc activation overpotential; κ is anisotropy free energy; α is the transfer coefficient; z is the valence of zinc ion; F is Faraday's constant; R is the ideal gas constant; T is electrolyte temperature. $G(\Upsilon) = W\Upsilon^2(1-\Upsilon)^2$ is a double-well free energy function without the electric field. $H(\Upsilon) = \Upsilon^3\left(6\Upsilon^2 - 15\Upsilon + 10\right)$ is an interpolating function of the liquid–solid interface.

$$\frac{\partial C}{\partial t} = \nabla\left(D(\Upsilon) \cdot \nabla C\right) - C \cdot \frac{\partial \Upsilon}{\partial t} \quad (2)$$

where C is the concentration of zinc ions in the electrolyte; D is the diffusivity of zinc ions.

$$\frac{\partial \Phi}{\partial t} = \lambda \frac{\partial \Upsilon}{\partial t} - \nabla\left(\sigma(\Upsilon) \cdot \nabla \Phi\right) \quad (3)$$

where Φ is electrolyte potential; σ is electrolyte conductivity; λ is the constant.

Energy density calculation

The assembled battery was measured for mass and size. The battery test recorded the capacity and energy value of ZAB in each cycle. The mass and volume of ZAB were calculated for energy density. The effeciencies of each cycle were calculated according to the charge capacity and discharge capacity(Jia et al., 2019, Majee et al., 2019, Xu et al., 2019b, Feng et al., 2020). It should be noted that the values were slightly affected by the previous cycles(Wang et al., 2018a). The current and capacity densities were calculated according to the area of OER electrodes(Tang et al., 2017, Pan et al., 2019, Guan et al., 2020, Wang et al., 2020).

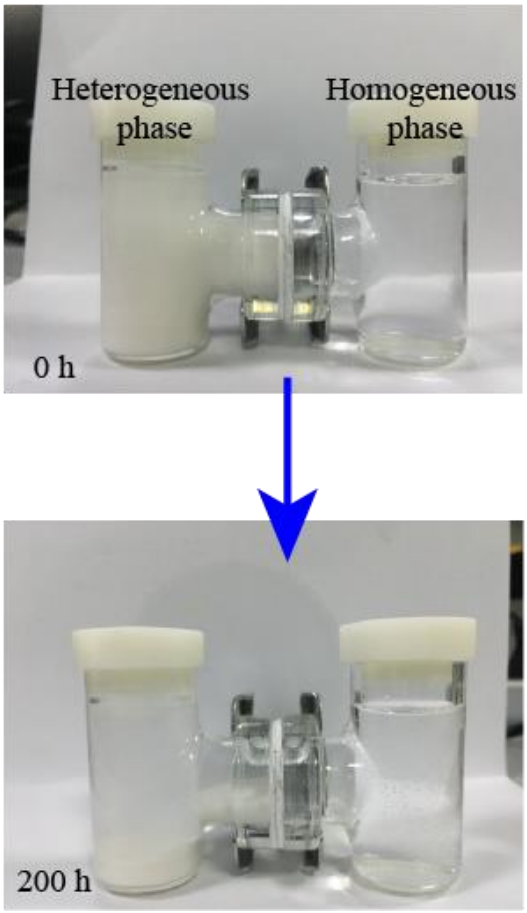

Figure S1. The durability of the hydrophilic PTFE membrane for separating the heterogeneous and homogeneous phases. Related to Figure 2.

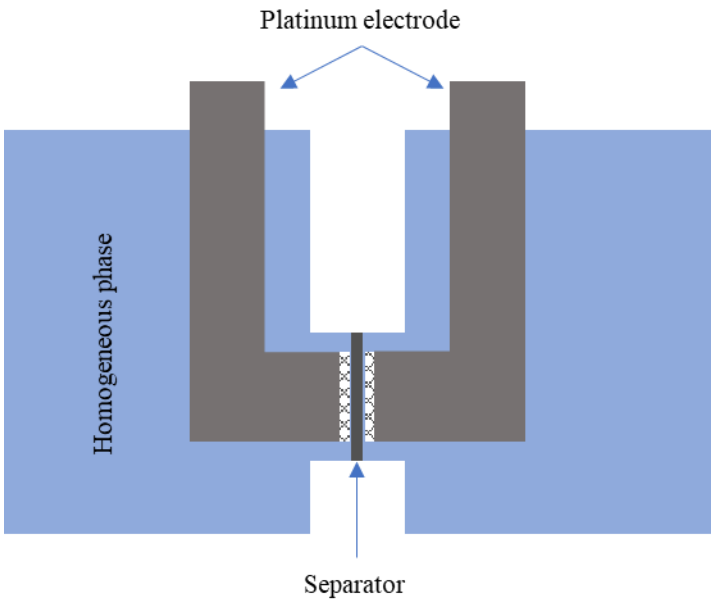

Figure S2. The diagrammatic sketch for measuring the impedance of the hydrophilic PTFE membrane in H-type electrolytic cell. Related to Figure 2.

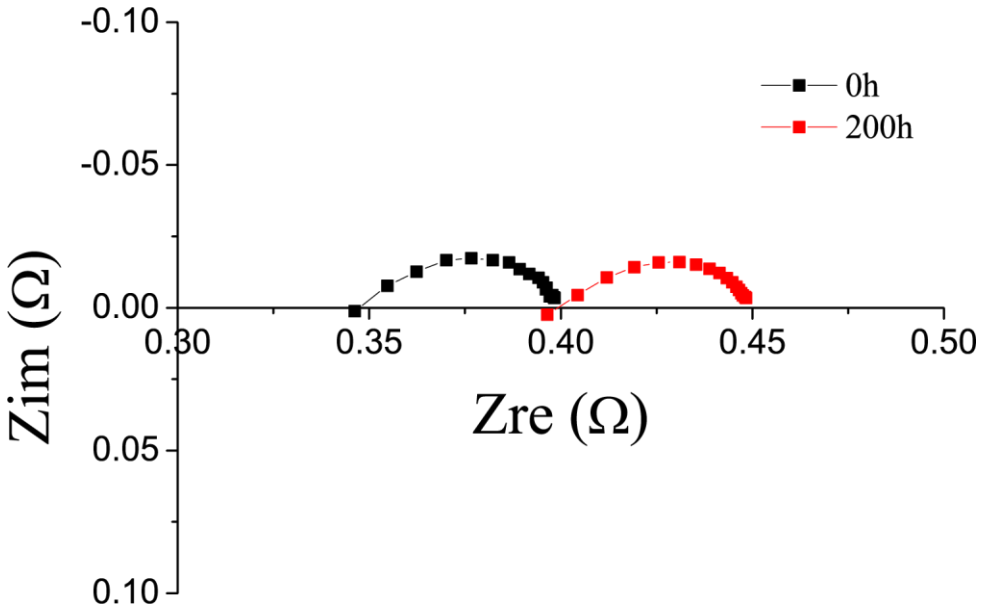

Figure S3. The change of the impedance of the hydrophilic PTFE membrane before (black dot) and after (red dot) durability test. Related to Figure 2.

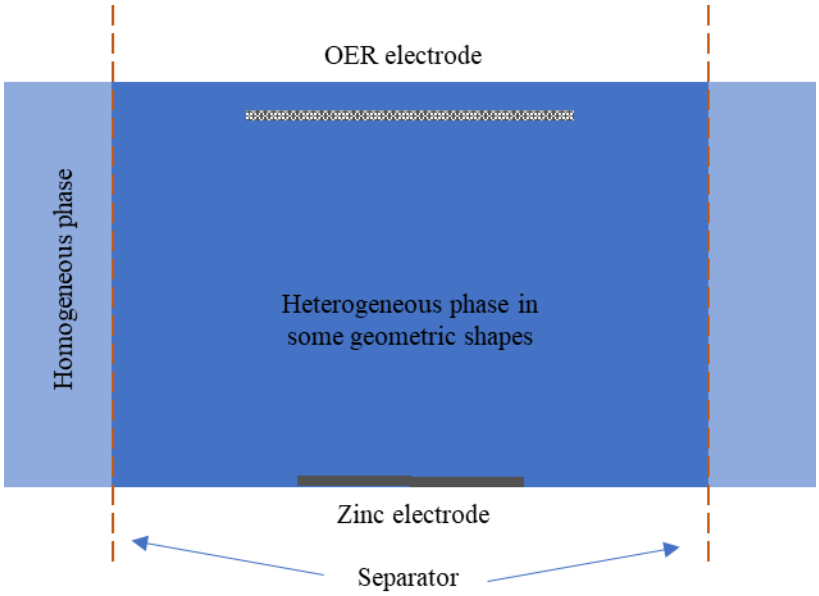

Figure S4. The diagrammatic sketch for the zinc deposition in the teterogeneous phase with some geometric shapes. Related to Figure 2.

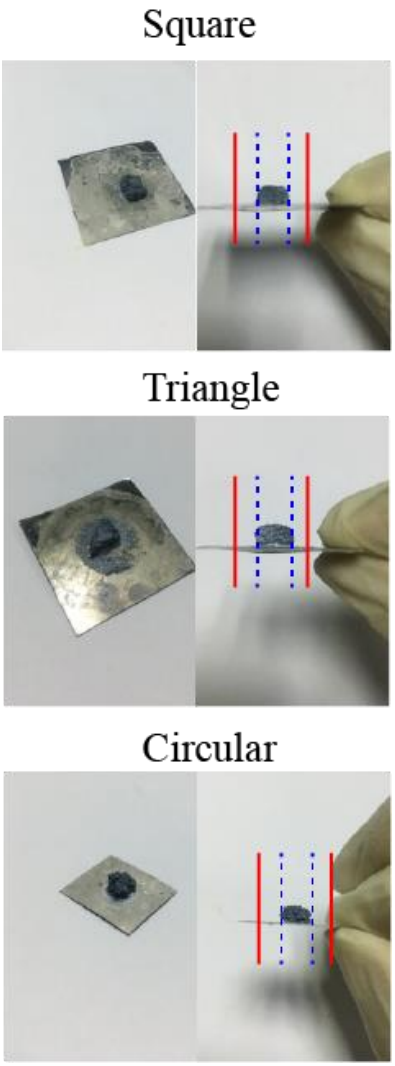

Figure S5. The macroscopic shapes of the zinc electrodeposit in the teterogeneous phase with some geometric shapes (in the blue dotted line); the red lines indicate the boundary of electrolytic cell. Related to Figure 2.

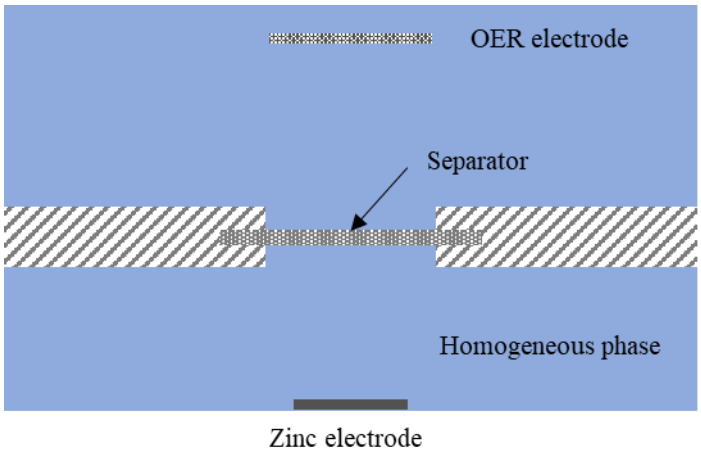

Figure S6. The diagrammatic sketch for the zinc electrodeposition with a separator between OER and zinc electrodes. Related to Figure 2.

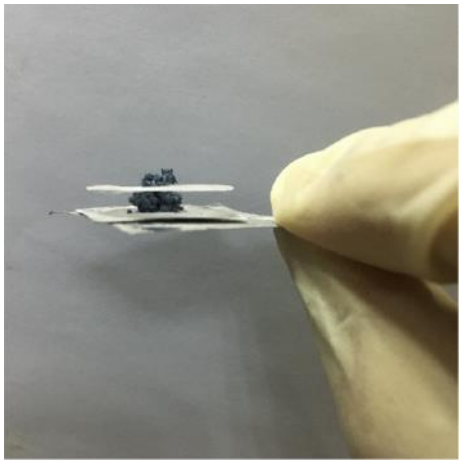

Figure S7. The macroscopic shapes of the zinc electrodeposit, crossing the separator between the OER and zinc electrodes. Related to Figure 2.

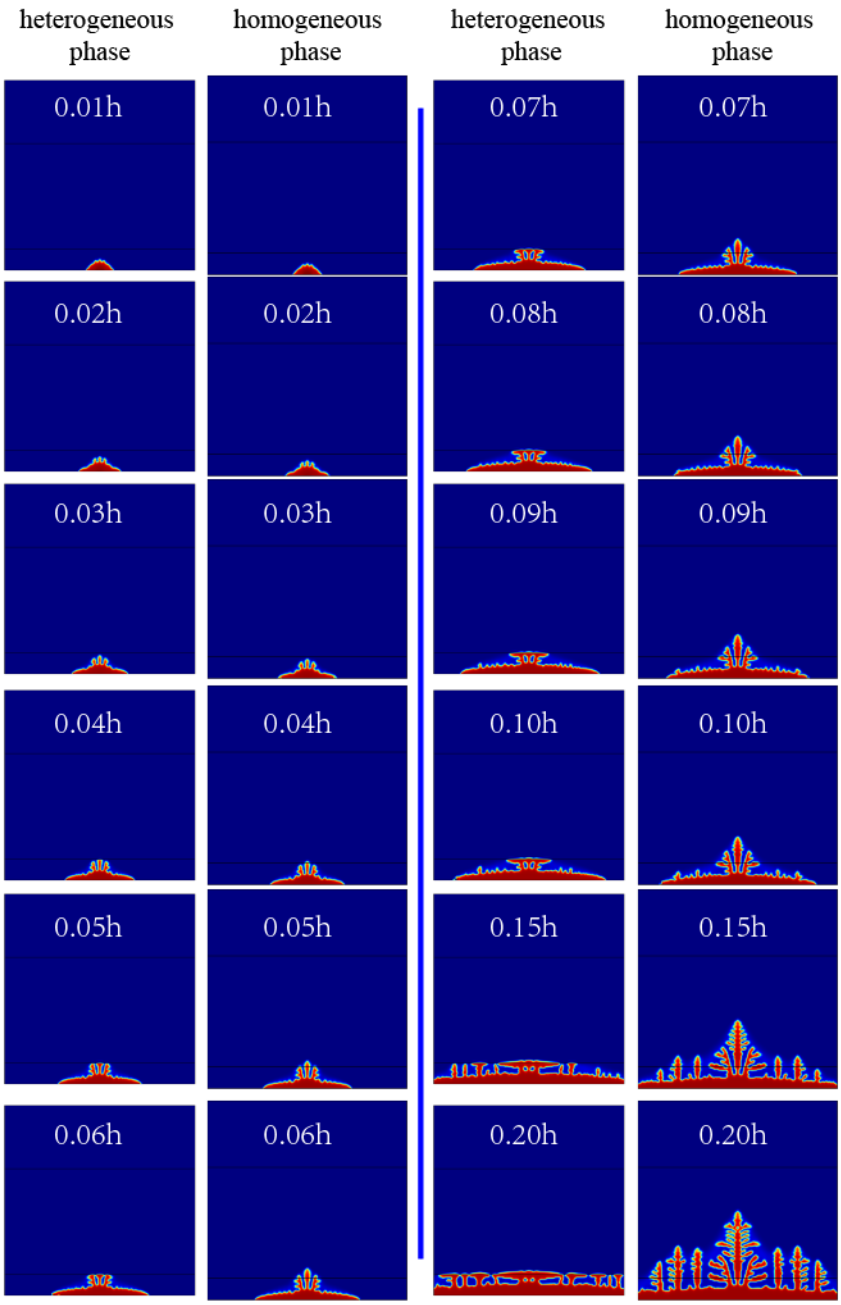

Figure S8. Simulation results of the zinc dendrite growing in the heterogeneous and homogeneous phases, the red and blue regions representing the metallic zinc and the electrolyte solution, respectively. Related to Figure 2.

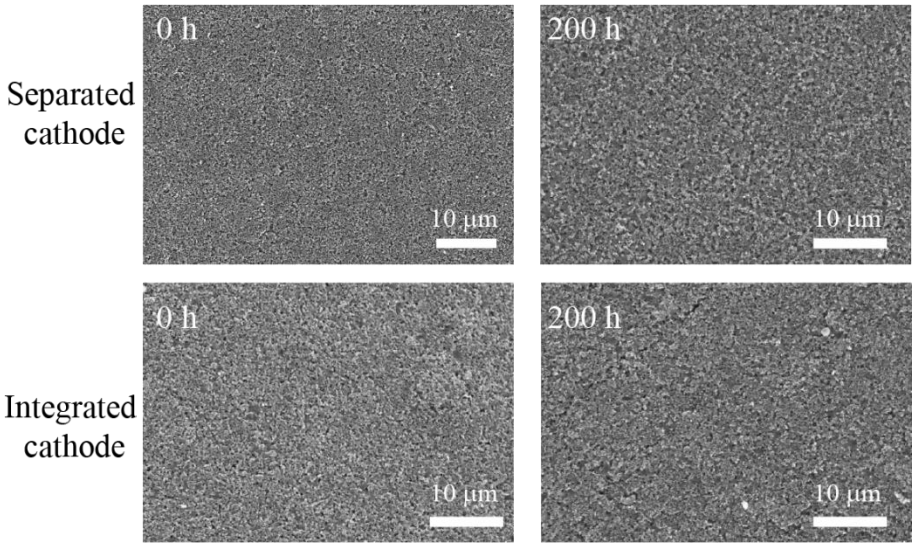

Figure S9. SEM images of both the separated and integrated air electrodes serving as cathode in a symmetrical electrolytic cell before and after the rectangular wave current test. Related to Figure 3.

Figure S10. The photograph and geometric characteristics of the ZAB. Related to Figure 4.

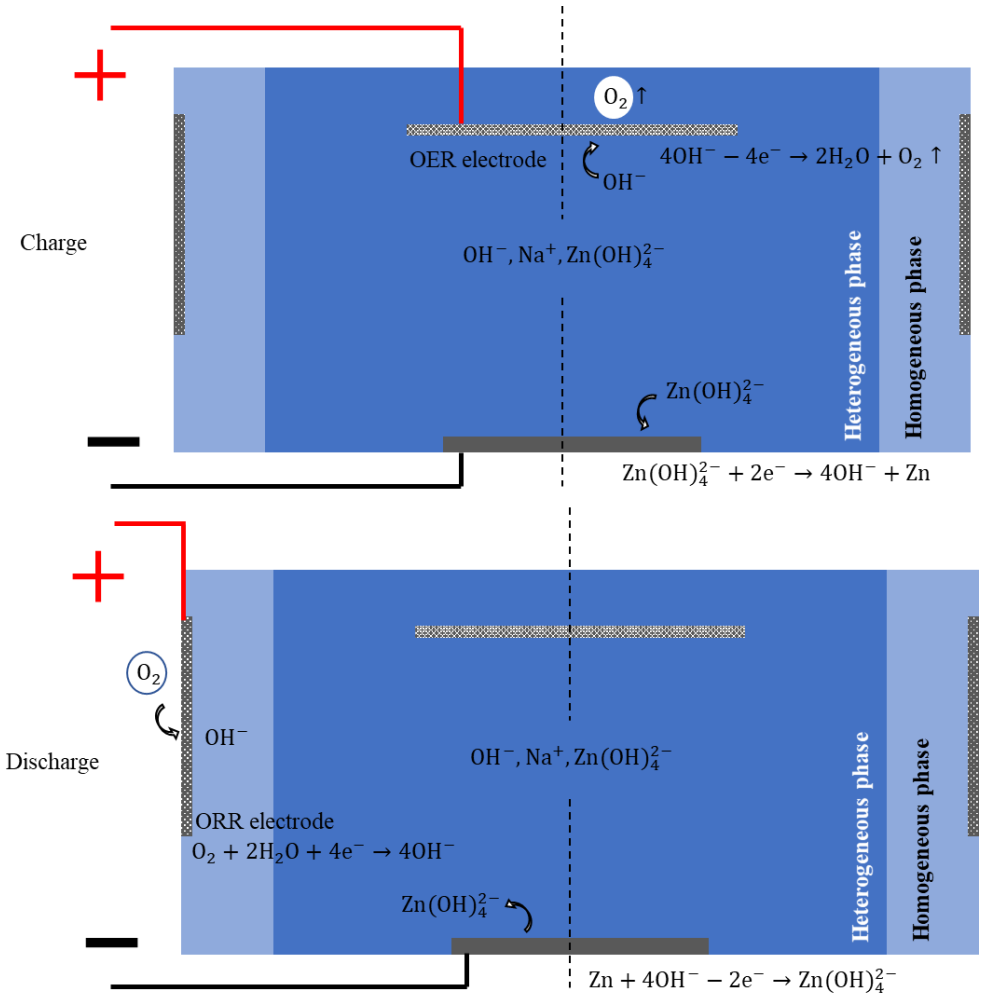

Figure S11. The electrical connection of the separated ORR/OER electrodes to the external load. Related to Figure 4.

Table S1. The ionic conductivity in different proportions of the ZnO in the multiphase electrolyte. Related to Figure 4.

Component	H_2O	NaOH	ZnO	Ionic conductivity/mS cm^{-1}
Proportion	1	1.2	0.1	160
	1	1.2	0.2	124
	1	1.2	0.4	80
	1	1.2	0.8	59

Table S2. The parameters of the full ZAB, including: battery container, multiphase electrolyte solution, air electrode and zinc electrode. Related to Figure 4.

Parameters of the ZAB	Diameter/mm	Height/mm	Volume/cm^3	Mass/g
Values	21.0	10.0	1.65	2.58

Table S3. Fundamental performance parameters of ZABs in recent research. Related to Figure 4.

Peak discharge power density (mW/cm^2)	energy density (based on zinc) mWh/g	energy density (based on battery) mW/cm^2 Wh/kg	cycle number	cycle time/h	Ref
291	-	-	140	100	(Guan et al., 2020)
-	-	-	5400	900	(Chen et al., 2020)
114	-	-	100	-	(Wu et al., 2019a)
160.6	-	-	960	640	(Wang et al., 2020)
-	776.3	-	-	100	(Majee et al., 2019)
-	-	-	320	107	(Feng et al., 2020)
162	827.5	-	-	425	(Wang et al., 2019b)
110.7	-	-	-	60	(Gao et al., 2019)
164	721(1V)	-	-	35	(Zhong et al., 2020)
70	-	-	150	25	(Wu et al., 2019b)
-	805(1V)	-	-	48	(Jia et al., 2019)
300	932.5	-	350	12	(Wang et al., 2019c)
-	866	-	500	-	(Xu et al., 2019b)
120	-	-	-	80	(You and Hu, 2018)
260	954.1	-	500	167	(Pan et al., 2019)

140	804(1V)	-	-	360	(Sun et al., 2020)
159.92	855.28	-	-	900	(Chen et al., 2020)
142.5	-	-	1050	350	(Li et al., 2020)
235	940	-	-	-	(Najam et al., 2019)
303.7	751.4(1V)	-	-	-	(Huo et al., 2019)
135	-	-	-	450	(Xing et al., 2019)
269.7		-	1288	215	(Liu et al., 2019)
534	770(1V)	-	540	135	(Xu et al., 2019a)
90	-	-	900	-	(Wang et al., 2018b)
55.1	-	-	75	-	(Ma and Wang, 2014)
340	775(1V)		504	84	(Li et al., 2017)
516.3	-	-	5000	23	(Tang et al., 2017)
320.2	**1050.9**	**196.2**	**10000**	**2000**	**This work**

References

Chen, C., Cheng, D., Liu, S., Wang, Z., Hu, M. and Zhou, K. 2020. Engineering the multiscale structure of bifunctional oxygen electrocatalyst for highly efficient and ultrastable zinc-air battery. *Energy Storage Materials,* 24**,** 402-411.

Feng, Q., Zhao, Z., Yuan, X.-Z., Li, H. and Wang, H. 2020. Oxygen vacancy engineering of yttrium ruthenate pyrochlores as an efficient oxygen catalyst for both proton exchange membrane water electrolyzers and rechargeable zinc-air batteries. *Applied Catalysis B: Environmental,* 260**,** 118176.

Fu, J., Cano, Z. P., Park, M. G., Yu, A., Fowler, M. and Chen, Z. 2017. Electrically rechargeable zinc–air batteries: progress, challenges, and perspectives. *Advanced materials,* 29**,** 1604685.

Gao, L., Zhu, M., Zhang, Z. and Cui, G. 2019. Cobalt-boron-oxide supported on N, P dual-doped carbon nanosheets as the trifunctional electrocatalyst and its application in rechargeable Zn-air battery and overall water-electrolysis. *Electrochimica Acta,* 327**,** 134980.

Guan, Z., Zhang, X., Fang, J., Wang, X., Zhu, W. and Zhuang, Z. 2020. Fe, Ni, S, N-doped carbon materials as highly active Bi-functional catalysts for rechargeable Zinc-Air battery. *Materials Letters,* 258**,** 126826.

Huo, M., Wang, B., Zhang, C., Ding, S., Yuan, H., Liang, Z., Qi, J., Chen, M., Xu, Y. and Zhang, W. 2019. 2D Metal–Organic Framework Derived CuCo Alloy Nanoparticles Encapsulated by Nitrogen-Doped Carbonaceous Nanoleaves for Efficient Bifunctional Oxygen Electrocatalyst and Zinc–Air Batteries. *Chemistry–A European Journal,* 25**,** 12780-12788.

Jia, N., Liu, J., Gao, Y., Chen, P., Chen, X., An, Z., Li, X. and Chen, Y. 2019. Graphene-encapsulated Co_9S_8 nanoparticles decorated N, S co-doped carbon nanotubes: An efficient bifunctional oxygen electrocatalyst for rechargeable zinc–air battery. *ChemSusChem*.

Li, W., Li, Y., Fu, H., Yang, G., Zhang, Q., Chen, S. and Peng, F. 2020. Phosphorus doped Co_9S_8@ CS as an excellent air-electrode catalyst for zinc-air batteries. *Chemical Engineering Journal,* 381**,** 122683.

Li, X., Xu, N., Li, H., Wang, M., Zhang, L. and Qiao, J. 2017. 3D hollow sphere Co_3O_4/MnO_2-CNTs: its high-performance bi-functional cathode catalysis and application in rechargeable zinc-air battery. *Green Energy Environment,* 2**,** 316-328.

Liu, C., Dong, F., Wu, M., Wang, Y., Xu, N., Wang, X., Qiao, J., Shi, P. and Huang, H. 2019. Dual-active-sites design of CoS_x anchored on nitrogen-doped carbon with tunable mesopore enables efficient Bi-Functional oxygen catalysis for ultra-stable zinc-air batteries. *Journal of Power Sources,* 438**,** 226953.

Ma, H. and Wang, B. 2014. A bifunctional electrocatalyst α-MnO_2-$LaNiO_3$/carbon nanotube composite for rechargeable zinc–air batteries. *RSC Advances,* 4**,** 46084-46092.

Majee, R., Islam, Q. A. and Bhattacharyya, S. 2019. Surface Charge Modulation of Perovskite Oxides at the Crystalline Junction with Layered Double Hydroxide for a Durable Rechargeable Zinc–Air Battery. *ACS applied materials interfaces,* 11**,** 35853-35862.

Najam, T., Shah, S. S. A., Ding, W., Deng, J. and Wei, Z. 2019. Enhancing by nano-engineering: Hierarchical architectures as oxygen reduction/evolution reactions for zinc-air batteries. *Journal of Power Sources,* 438**,** 226919.

Pan, Z., Yang, J., Zang, W., Kou, Z., Wang, C., Ding, X., Guan, C., Xiong, T., Chen, H. and Zhang, Q. 2019. All-solid-state sponge-like squeezable zinc-air battery. *Energy Storage Materials*.

Sun, H., Li, Q., Lian, Y., Zhang, C., Qi, P., Mu, Q., Jin, H., Zhang, B., Chen, M. and Deng, Z. 2020. Highly efficient water splitting driven by zinc-air batteries with a single catalyst incorporating rich active species. *Applied Catalysis B: Environmental,* 263**,** 118139.

Tang, Q., Wang, L., Wu, M., Xu, N., Jiang, L. and Qiao, J. 2017. Achieving high-powered Zn/air fuel cell through N and S co-doped hierarchically porous carbons with tunable active-sites as oxygen electrocatalysts. *Journal of Power Sources,* 365**,** 348-353.

Wang, F., Borodin, O., Gao, T., Fan, X., Sun, W., Han, F., Faraone, A., Dura, J. A., Xu, K. and Wang, C. 2018a. Highly reversible zinc metal anode for aqueous batteries. *Nature materials,* 17**,** 543.

Wang, H.-F., Tang, C., Wang, B., Li, B.-Q., Cui, X. and Zhang, Q. 2018b. Defect-rich carbon fiber electrocatalysts with porous graphene skin for flexible solid-state zinc–air batteries. *Energy Storage Materials,* 15**,** 124-130.

Wang, K., Xiao, Y., Pei, P., Liu, X. and Wang, Y. 2019a. A Phase-Field Model of Dendrite Growth of Electrodeposited Zinc. *Journal of The Electrochemical Society,* 166**,** D389-D394.

Wang, P., Wan, L., Lin, Y. and Wang, B. 2019b. Construction of mass-transfer channel in air electrode with bifunctional catalyst for rechargeable zinc-air battery. *Electrochimica Acta,* 320**,** 134564.

Wang, T., Wu, J., Liu, Y., Cui, X., Ding, P., Deng, J., Zha, C., Coy, E. and Li, Y. 2019c. Scalable preparation and stabilization of atomic-thick CoNi layered double hydroxide nanosheets for bifunctional oxygen electrocatalysis and rechargeable zinc-air batteries. *Energy Storage Materials,* 16**,** 24-30.

Wang, Z., Ang, J., Liu, J., Ma, X. Y. D., Kong, J., Zhang, Y., Yan, T. and Lu, X. 2020. FeNi alloys encapsulated in N-doped CNTs-tangled porous carbon fibers as highly efficient and durable bifunctional oxygen electrocatalyst for rechargeable zinc-air battery. *Applied Catalysis B: Environmental,* 263**,** 118344.

Wu, M., Guo, B., Nie, A. and Liu, R. 2019a. Tailored architectures of FeNi alloy embedded in N-doped carbon as bifunctional oxygen electrocatalyst for rechargeable Zinc-air battery. *Journal of colloid interface science*.

Wu, X., Chen, S., Feng, Y., Yuan, Q., Gao, J., Chen, Y., Huang, Y., He, Y.-B. and Gan, W. 2019b. Microwave-assisted synthesis of carbon nanotubes threaded core-shell CoP_x/Co-N_x-C@ CNT and its performance as an efficient bifunctional oxygen catalyst for the rechargeable zinc-air battery. *Materials Today Physics,* 9**,** 100132.

Xing, Z., Deng, Y.-P., Sy, S., Tan, G., Li, A., Li, J., Niu, Y., Li, N., Su, D. and Lu, J. 2019. Carbon-pore-sheathed cobalt nanoseeds: An exceptional and durable bifunctional catalyst for zinc-air batteries. *Nano Energy,* 65**,** 104051.

Xu, N., Zhang, Y., Wang, M., Fan, X., Zhang, T., Peng, L., Zhou, X.-D. and Qiao, J. 2019a. High-performing rechargeable/flexible zinc-air batteries by coordinated hierarchical Bi-metallic electrocatalyst and heterostructure anion exchange membrane. *Nano Energy,* 65**,** 104021.

Xu, R., Luo, F., Li, M. and Yang, Z. 2019b. Ultrafine cobalt nitride nanoparticles supported on carbon nanotubes as efficient electrocatalyst for rechargeable zinc–air batteries. *Chemical Communications,* 55**,** 13394-13397.

You, T.-H. and Hu, C.-C. 2018. Designing Binary Ru–Sn Oxides with Optimized Performances for the Air Electrode of Rechargeable Zinc–Air Batteries. *ACS applied materials interfaces,* 10**,** 10064-10075.

Zhong, X., Yi, W., Qu, Y., Zhang, L., Bai, H., Zhu, Y., Wan, J., Chen, S., Yang, M. and Huang, L. 2020. Co single-atom anchored on Co_3O_4 and nitrogen-doped active carbon toward bifunctional

catalyst for zinc-air batteries. *Applied Catalysis B: Environmental,* 260**,** 118188.